

ASCA OBSERVATIONS OF THE IONIZED GAS IN THE SEYFERT GALAXY NGC 3783

I.M. George^{1,2}, T.J. Turner^{1,2}, R. Mushotzky¹, K. Nandra^{1,3}, H. Netzer⁴

ABSTRACT

We present the results from *ASCA* observations of NGC 3783 carried out during 1993 and 1996. Variability is observed both between the two epochs and within the individual observations, the latter due to a non-stationary process.

We find the spectra at both epochs to contain features due to absorption by ionized material, predominantly due to OVII and OVIII. We find the opacity for such material to decrease by a factor ~ 2 in the ~ 0.7 – 1.0 keV band between the epochs while the photoionizing flux increases by $\sim 25\%$. By comparison with detailed photoionization models we show this behaviour is inconsistent with that expected from a single-zone of photoionized gas. A deficit in the data compared to such models, consistent with excess absorption by OVIII, supports the suggestion that the material consists of two or more zones

Significant Fe *K*-shell emission is also observed during both epochs. We show this emission is dominated by the asymmetric line profile expected from the innermost regions of the accretion flow. We find no evidence that the Fe emission varied in either shape or equivalent width between the two epochs.

Subject headings: galaxies:active – galaxies:nuclei – galaxies:Seyfert – galaxies:individual (NGC 3783) – X-rays:galaxies

¹Laboratory for High Energy Astrophysics, Code 660, NASA/Goddard Space Flight Center, Greenbelt, MD 20771

²Universities Space Research Association

³NAS/NRC Research Associate

⁴School of Physics and Astronomy and the Wise Observatory, The Beverly and Ramond Sackler Faculty of Exact Sciences, Tel Aviv University, Tel Aviv 69978, Israel.

1. INTRODUCTION

The almost face-on spiral (SBa) galaxy NGC 3783 ($z = 0.0097$) is one of the brighter Seyfert galaxies in the sky in all wavebands (e.g. Alloin et al. 1995 and references therein). At X-ray wavelengths, NGC 3783 was first detected in the *Ariel-V* sky-survey and has subsequently been observed by all major X-ray instruments (e.g. Malizia et al 1997 and references therein). Evidence for deep absorption features in the 0.5–1.5 keV band was first obtained in a *ROSAT* observation (Turner et al. 1993) and confirmed in a subsequent *ASCA* observation (George, Turner & Netzer 1995, hereafter G95). The latter workers demonstrated the opacity was dominated by *K*-shell absorption edges due to OVII and OVIII within a screen of material (with an effective hydrogen column density $\sim 10^{22}$ cm $^{-2}$) within the column-of-sight to the central source of X-ray emission. Subsequent *ASCA* observations have revealed such screens of photoionized material (so-called "warm absorbers") to be a common features in Seyfert galaxies (Reynolds 1997; George et al 1998a, hereafter G98). G95 also suggested the tentative detection of the emission predicted to arise from within such a screen of ionized gas if it subtends a significant solid angle at the central source.

Here we present the results from the analysis of four new *ASCA* observations of NGC 3783 performed in 1996 July, along with a re-analysis of the two previous observations carried out in 1993 December (and as reported previously by G95, Reynolds 1997 and G98). The observations performed in 1996 were each separated by ~ 2 days, with the hope (based on the behaviour seen during 1993) of measuring the reaction of the ionized screen to changes in the illuminating continuum, and hence better constrain the location of and physical conditions within the screen. Unfortunately, the photoionizing source did not co-operate, exhibiting only relatively low-amplitude variations during the 1996 observations. However, we as we shall show, useful insights regarding the nature of the ionized, circumnuclear material can still be obtained by comparison of the 1996 and 1993 observations.

The observations and data-screening employed are described in §2. In §3 we describe the results of our spatial and temporal analysis. The results of our spectral analysis of the absorption due to the ionized gas are presented in §4, confirming the presence of the ionized material during both 1993 and 1996. However we find the opacity of the ionized material to decrease by a factor ~ 2 between these epochs, and discuss physically realistic explanations. In §5 we discuss the constraints which can be placed on the emission due to Fe *K*-shell processes in the 5–7 keV band. Finally, in §6 we review our findings in the context of the results from similar objects and future observations.

2. OBSERVATIONS AND DATA REDUCTION

ASCA consists of four identical, co-aligned X-ray telescopes (XRTs; Serlemitsos et al. 1995). Two solid-state imaging spectrometers (known as SIS0 and SIS1), each consisting of four CCD chips, sit at the focus of two of the XRTs, and provide coverage over the $\sim 0.4\text{--}10$ keV band (Burke et al. 1994). Two gas imaging spectrometers (known as GIS2 and GIS3) sit at the focus at the focus of the other two XRTs, and provide coverage over the $\sim 0.8\text{--}10$ keV band (Ohashi et al. 1996). Further details on the satellite, its instrumentation and performance can be found in Makishima et al. (1996) and references therein.

The four new observations of NGC 3783 reported here were carried out over the period 1996 July 09–16. We have also performed a re-analysis of the 2 observations of NGC 3783 carried out in 1993 December 19–23, which have been previously described in G95, Reynolds (1997) and G98. However, here we utilize raw data from the `Rev2` processing⁵, along with new screening criteria and the latest calibration files. These changes result in slightly different values for some parameters compared to previously published results. The full observing log is given in Table 1.

The data-selection and screening criteria used here are similar to those described in Nandra et al (1997a). We started from the ‘unscreened’ event files. Data collected in `FAINT` and `BRIGHT` data modes were combined, as were data obtained during all three telemetry modes. These data were then screened⁶ using the `ASCASCREEN/XSELECT` script (v0.43) within the `FTOOLS` package (v3.6) such as only to include data collected when: the spacecraft was outside of the South Atlantic Anomaly; the radiation belt monitor rate was less than 500 ct s^{-1} ; magnetic cut-off rigidity was $>6 \text{ GeV/c}$; angular offset from the the nominal pointing position was $<36 \text{ arcsec}$; elevation angle above the Earth’s limb was $> 5^\circ$ for GIS data, and $> 10^\circ$ for SIS data. In the case of SIS data (only), the following additional criteria were applied: that the Bright Earth angle (elevation angle above the sun-illuminated Earth’s limb) was $> 20^\circ$; that the spacecraft was at least 100 s beyond the day/night terminator; that the CCD pixel threshold was <100 (<75 for the 1993 observations). ‘Hot’ and ‘flickering’ pixels were removed from the SIS using the standard algorithm. Only SIS ‘grades’ 0, 2, 3 and 4 were included in the analysis. The original pulse-height assignment for each event was converted to a pulse-invariant (PI) scale using `SISPI` (v1.1). In the case of the GIS data (only), the recently-discovered method of rejecting ‘hard particle flares’ using the so-called `H02` count rate was employed, as was the standard

⁵hence raw data from the same processing configuration (6.4.2) is used for all the datasets

⁶the ‘mkf-file’, describing the orbital parameters of the satellite, was corrected for the errors in the version initially used during the pre-processing of the 1996 datasets

‘rise-time’ criteria. It should be noted that these screening criteria are more conservative than those used in G95 and resulted in lower effective exposure times of ~ 17 ks and ~ 15 ks in each instrument for the Dec 19 and Dec 23 observations (respectively).

3. SPATIAL & TEMPORAL ANALYSIS

Images were extracted for each instrument during each observation. In all cases, a bright source was detected with an X-ray centroid consistent with the optical position of NGC 3783 to within the uncertainty in the positional accuracy of the *ASCA* attitude reconstruction (90% confidence radius of 40 arcsec, Gotthelf & Ishibashi 1997).

No serendipitous sources were detected which are likely to contaminate significantly the analysis of the target. Analysis of the archival *ROSAT* observation (that made in 1993 June) using the Position Sensitive Proportional Counter (PSPC) in the focal plane reveals no evidence for extended emission.

3.1. Extraction Cells

Extraction cells were defined for the subsequent temporal and spectral analysis. In the case of the SIS data, the source region employed was circular of radius ~ 3.2 arcmin centered on NGC 3783. From the nominal point-spread function (psf) of the XRT/SIS instrument, such a region contains $\sim 84\%$ of the total source counts. For the count rate and spectrum of NGC 3783, we find the background (instrumental and diffuse X-ray background) within the source region to be $\gtrsim 10\%$ of the observed source flux $\gtrsim 5$ keV. Thus an extraction cell was defined to provide an estimate of the background for each SIS detector which consisted of the whole CCD chip excluding a circular region of ~ 4.3 arcmin centered on the source. In the case of the GIS data, the source region was circular of radius ~ 5.2 arcmin centered on NGC 3783. From the psf of the XRT/GIS instrument such a region contains $\sim 89\%$ of the total source counts. The GIS has a higher background than the SIS, contributing $\gtrsim 10\%$ of the observed source flux $\lesssim 1$ keV and $\gtrsim 4$ keV. Thus an annulus, centered on the source and covering ~ 5.2 – 9.8 arcmin was used to provide an estimate of the background for each GIS detector. All fluxes and luminosities quoted below (*not* count rates) have been corrected for the fraction of the source photons falling outside the source extraction cells and for the contamination of source counts in the background extraction cells ($\sim 6\%$ and $\sim 11\%$ of the source counts for the XRT/SIS and XRT/GIS instruments respectively).

3.2. Variability Studies

Light curves were constructed for the source and background regions for several different energy ranges for each detector during each observation. To increase the signal-to-noise ratio, the light curves from SIS0 and SIS1 and from GIS2 and GIS3 were combined in each case. The light curves were then rebinned on a variety of timescales.

In Fig. 1 we show the light curves for the 0.5–10 keV SIS and 2–10 keV GIS with a bin size of 5760 s (approximated the orbital period of the *ASCA*). Variability is apparent both between and within individual observations. From Fig. 1 and Table 1 it can be seen that the mean count rate during the 1996 observations is a factor ~ 1.5 higher than during the 1993 observations. The softness ratio, shown in the lower panel of Fig. 1, exhibited a clear increase between the 1993 and 1996 observations. As we shall show below, this primarily due to a decrease in the opacity of ionized material between the two epochs.

Interestingly NGC 3783 is seen to exhibit significant variability during in all but one (Obs. c) of the observations. In Table 2 we list the normalised 'excess variance', σ_{rms}^2 , of each light curve using the prescription⁷ given in Nandra et al (1997a). We find no significant differences between σ_{rms}^2 from the light curves constructed in the hard (2–10 keV) and soft (0.5–2 keV) bands. This is confirmed by the lack of significant intra-observation variability seen in the softness ratio. However, there are clear variations in σ_{rms}^2 from observation to observation. For all four bands we find σ_{rms}^2 inconsistent with a constant at $>99\%$ confidence, indicating the process responsible for the variability is not stationary.

4. SPECTRAL ANALYSIS EXCLUDING THE IRON *K*-SHELL EMISSION

Given the lack of large-amplitude variability within each observation (Fig. 1), here we consider the mean spectra for each observation. Source and background spectra were extracted from the cleaned event list of each detector using the extraction cells described in §3.1. For the SIS datasets, appropriate detector redistribution matrices were generated using `sisrmg` (v1.1). For the GIS datasets the redistribution matrices released on 1995 Mar 06 (generated by `gisres` v4.0) were used. Ancillary response files were generated for all detectors using `ascaarf` (v2.72).

In all cases described below, the spectral analysis is performed on the data from all four

⁷We note there is a typographical error in the expression for the error on σ_{rms}^2 given in Nandra et al (1997a), whereby the expression within the summation should be squared.

instruments simultaneously, with different relative normalizations to account for (small) uncertainties in the determination of their effective areas. (The correction for the fraction of the source counts falling outside the source region used for each detector is corrected for within `ascaarf`.) Data below 0.6 keV were excluded from the spectral analysis as it is commonly accepted that there are uncertainties associated with the calibration of the XRT/SIS system below this energy. However, whilst the calibration is suspect at these energies, it is considered unlikely to be in error by $\gtrsim 20\%$.

The individual spectra were grouped such as to contain a minimum of 20 counts per new bin, and hence allowing χ^2 minimization techniques to be employed within the XSPEC (v10.00) spectral analysis package. For all the analysis presented in this section, we have assumed spectral models consisting of an underlying power-law continuum (of photon index Γ) absorbed by a neutral column ($N_{H,0}$) at zero redshift. We assume a Galactic column density of $N_{H,0}^{gal} = 8.7 \times 10^{20} \text{ cm}^{-2}$ ($E(B - V) = 0.12$ for a Galactic gas-to-dust ratio) along the column-of-sight to NGC 3783, as derived from the fits of the *HST* FOS spectrum (Allion et al. 1995), and consistent with the 21 cm measurements in this direction (Stark et al. 1992). Unless stated otherwise, we fix $N_{H,0} = N_{H,0}^{gal}$ in the spectral analysis presented below.

As will be discussed in §5, a strong emission line is present in the spectrum of NGC 3783 during all observations as a result of Fe *K*-shell fluorescence. The best-fitting parameters of such a line are dependent upon the form of the underlying continuum, which itself is highly correlated with the absorption present in the soft X-ray band. In this section, we exclude the 5–7 keV band (source frame) from our analysis and concentrate on the form of the continuum and the nature of the absorber. The characteristics of the emission line and its (small) effect on the properties of the continuum and absorption are postponed to §5.

4.1. The ION models

Strong absorption features are clearly evident within the 0.6–3 keV band of all six datasets. Models including photoionized material within the column-of-sight to NGC 3783 have been suggested previously to offer the most viable explanation for such features in this and other Seyfert 1 galaxies. Thus we start by considering such a model, based on detailed photoionization calculations.

We employ the same photoionization calculations used by G98. Model spectra were generated using the photoionization code ION (version ION96) to calculate the physical state of a slab of gas when illuminated by an ionizing continuum (Netzer 1993, 1996).

The code includes all important excitation and ionization processes, full temperature and radiative transfer solutions, and emission, absorption and reflection by the gas are calculated self-consistently assuming thermal and ionization equilibrium. We assume an illuminating continuum typical of AGN of the luminosity of NGC 3783 (the ‘weak IR’ case of Netzer 1996, except for the spectral index in the X-ray band), solar abundances and a density of $n = 10^{11} \text{ cm}^{-3}$. Following Netzer (1996) and G98, the intensity of the ionizing continuum is parameterized by the ‘X-ray ionization parameter’, U_X , defined as

$$U_X = \int_{0.1 \text{ keV}}^{10 \text{ keV}} \frac{Q(E)}{4\pi r^2 n c} dE \quad (1)$$

where $Q(E)$ is the rate of photon emission at energy E , r the distance from the source to the illuminated gas. Further details on the assumptions made in the ION models, the method by which they were included in the spectral analysis, and conversion factors between U_X and ionization parameters defined over the entire photoionizing continuum ($>13.6 \text{ eV}$) for various spectral forms can be found in G98.

4.2. Results assuming a single-zone ionized-absorber

Assuming a single powerlaw continuum, absorbed by a screen of ionized material at the redshift of the source ($N_{H,z}$), and by a screen of neutral material at $z = 0$ ($N_{H,0}$), in all cases we found $N_{H,0}$ consistent with $N_{H,0}^{gal}$. Thus the analysis was repeated with $N_{H,0}$ fixed at this value. The results are listed in Table 3, and the contours of the 90% confidence regions in the $N_{H,z}$ - U_X and $N_{H,z}$ - Γ planes are shown in Fig 2.

For reasons which will become apparent, we first consider the four datasets taken during the 1996 epoch, then compare these results to those from the datasets obtained during 1993.

4.2.1. The 1996 observations

From Table 3, it can be seen that the single-zone photoionization model provide fits which are deemed acceptable for all 4 datasets obtained during the 1996 epoch (with $P < 0.95$ and $0.8 \leq \overline{R_{0.6}} \leq 1.2$, see table notes). Indeed, as is clearly demonstrated in Fig 2, the best-fitting parameters are all consistent with an underlying continuum with $\Gamma \simeq 1.74$, absorbed by a screen of ionized material with $N_{H,z} \simeq 1.3 \times 10^{22} \text{ cm}^{-2}$ and $U_X \simeq 0.14$. The intensity of the photoionizing source does exhibit statistically significant variations between the four observations. However these are of relatively low amplitude (Fig. 1).

For example, the implied luminosity over the 0.5–2.0 keV band, $L_{0.5-2}$ has a mean value $\langle L_{0.5-2} \rangle_{96} = 2.07 \times 10^{43}$ erg s⁻¹ during 1996, and exhibits variability $\lesssim 10\%$ between the observations (Table 3).

We have repeated the spectral analysis, but simultaneously fitting the data from all four detectors and all four observations obtained during 1996, again allowing the relative normalizations to vary. We find best-fitting values of $\langle N_{H,z} \rangle_{96} = 1.32_{-0.06}^{+0.07} \times 10^{22}$ cm⁻², $\langle U_X \rangle_{96} = 0.138_{-0.006}^{+0.006}$, and $\langle \Gamma \rangle_{96} = 1.73_{-0.01}^{+0.02}$, in excellent agreement with the values anticipated from Table 3. (For reference, for the assumed XUV spectrum, $\langle U_X \rangle_{96}$ corresponds to an ionization parameter integrated over all energies >1 Ryd of $U = 19.5$.) The spectrum implied by these observations is shown in the upper panel of Fig. 3. From the mean data/model ratios shown in the lower panel of Fig. 3, noticeable discrepancies between the data and model occur at four locations within the spectrum. The most significant feature — an excess of observed counts compared to the model in the 5–7 keV band — is of course that expected due to Fe *K*-shell emission, and is discussed in §5. Two additional features are also anticipated and due to instrumental discrepancies. These are the deficit of observed counts < 0.6 keV (with an amplitude data/model $\overline{R}_{0.6} \sim 0.9$) consistent with accepted inaccuracies in the calibration of the XRT/SIS instrument at these energies, and the feature in the 2–3 keV band due to slight errors in the modelling of the *M*-shell features in the Au coating the XRTs. The final discrepancy is the deficit of observed counts compared to the model in the 0.8–1 keV band and has an astrophysically-interesting interpretation, lying in a spectral band where there are no known problems with the calibrations of the instruments. We postpone further discussion of this ‘1 keV deficit’ to §4.3.

To summarize, the basic conclusion is that over the week of the 1996 observations, the underlying continuum in NGC 3783 was consistent with a constant spectral index of $\langle \Gamma \rangle_{96}$ and exhibited only low-amplitude variations in X-ray luminosity. The bulk of the opacity evident during these observations is due to the column-of-sight to the central source being covered by a screen of ionized material of constant column density ($\langle N_{H,z} \rangle_{96}$), density and radius (giving rise to $\langle U_X \rangle_{96}$). The lack of large-amplitude variations in the underlying continuum, combined with the achievement of statistically-acceptable fits using the ION models, indicates the ionized material is consistent with being approximately in ionization equilibrium.

4.2.2. The 1993 observations

The simplest scenario one can anticipate is that during the 1993 observations the column-of-sight to NGC 3783 is covered by the same screen of material as that present during the 1996 observations (i.e. with $\langle N_{H,z} \rangle_{96}$), but that the level of ionization in this material is lower due to the reduction in the ionizing luminosity during the earlier epoch. However we find this not to be the case. This is demonstrated in Fig 4 in which we show the data/model residuals to the 1993 datasets under the assumption that the ionized material has $\langle N_{H,z} \rangle_{96}$, that the underlying spectral index is the same at both epochs ($\langle \Gamma \rangle_{96}$), and the ionization parameter during the 1993 observations is lower by a factor proportional to that implied by the luminosity of the photoionizing continuum. Since incident photons with energies in the 0.5–2.0 keV dominate the ionization structure of highly-ionized species of O, we have rescaled U_X assuming $U_X = \langle U_X \rangle_{96} (L_{0.5-2} / \langle L_{0.5-2} \rangle_{96})$ for Fig 4. Large deficits are clearly evident in the residuals, clearly indicating extra opacity during the 1993 observations. Thus we can reject the hypothesis that the same column of gas is in equilibrium during the 1993 and 1996 observations with its ionization structure simply reflecting the change in ionizing continuum between the epochs.

The next simplest scenario is that during both the 1993 and 1996 observations there is a single zone, in equilibrium, fully covering the cylinder-of-sight, however the column density, density and/or radius of this material is different during the two epochs. This might be the case if, for example, the circumnuclear material is inhomogeneous on large scales (greater than the size of the central source) and exhibits transverse motion. A different screen of material might then lie within the cylinder-of-sight during the two epochs. However, from Table 3, it can be seen that the single-zone photoionization model does not provide a statistically acceptable description to the 2 datasets obtained during the 1993 epoch. The spectra implied by these observations are shown in Fig. 5, along with the mean data/model ratios. We consider the inadequacy of the single-zone fits an indication that the true physical situation is yet more complex.

4.3. Resolving the discrepancy

We observed that in NGC 3783, the opacity of the warm-absorber decreased between the 1993 and 1996 epochs, while the source luminosity increased. We have also observed a deficit in the data at ~ 1 keV during both epochs compared to the expectations of our ionized-absorber model. Furthermore, comparison of Figs. 3 and 5 reveals that this deficit appears more pronounced during the 1993 observations when the implied column density of ionized material is larger. In this section we discuss several possible explanations for these

observable properties.

4.3.1. *Is the 1 keV Deficit an Instrumental Artifact ?*

There are no *known* problems with the calibration of the instruments at ~ 1 keV during the epochs of these observations (Yaqoob, p.comm). In addition, as noted in G98, the 1 keV deficit appear to be seen only in the sources with strong absorption features due to ionized gas (e.g. NGC 3516, MCG-6-30-15), and yet not seen in sources with no evidence for absorption by ionized gas (e.g. 3C 120). Thus, whilst a currently-unknown instrumental artifact cannot be completely excluded as the cause of the feature, such an explanation requires an unlikely conspiracy of a time-dependent phenomenon.

4.3.2. *Could the Atomic Cross-sections be Inaccurate ?*

The absorption cross-sections used here were based on the analytical fits to the theoretical calculations of Verner & Yakovlev (1995). These generally agree very well with other calculations and measurements, giving threshold cross-sections of $2.4 \times 10^{-19} \text{ cm}^2$ and $9.9 \times 10^{-20} \text{ cm}^2$ for OVII(739 eV) and OVIII(871 eV), respectively. However, if these values were in error (e.g. if the assumed cross-section for OVIII(871 eV) has been significantly underestimated whilst that for OVII(739 eV) is correct) this might lead to deficit similar to that observed.

In order to investigate this further, we have parameterized the 1 keV deficit using an additional absorption edge with a threshold fixed at a rest-frame energy of 871 eV. The results are listed in Table 4. It can be seen that both the 1993 datasets give a best-fitting column of $N_{H,z} = 1.7 \times 10^{22} \text{ cm}^{-2}$ and $\tau \sim 0.5$, while the analysis of the combined 1996 datasets give a best-fitting column of $N_{H,z} = 1.1 \times 10^{22} \text{ cm}^{-2}$ and $\tau \sim 0.15$. Thus the cross-section of OVIII(871 eV) would have to have been underestimated by a factor of ~ 2 or 3 (or the cross-section of OVII(739 eV) overestimated by these factors) in order to account for the size of the observed deficit. We consider such an explanation unlikely.

4.3.3. *Is the gas out of equilibrium or turbulent ?*

Our ION models assume that the ionized material is in photoionization equilibrium. If this is not the case, then we might expect imperfect spectral fits and deviations of the data compared to the best-fitting model. The fact that the 1 keV deficit appears more

marked in the 1993 observations would suggest the gas might be further from equilibrium during that epoch. Furthermore we note that the underlying continuum exhibited marked downward trends during both the 1993 observations (Fig. 1), which might be considered circumstantial evidence for such an hypothesis.

In the absence of other sources of heating and cooling, the gas will be in photoionization equilibrium if the photoionization and recombination timescales of the dominant species are shorter than the variability timescale (t_{var}) of the illuminating continuum. To first order $t_{ion} \simeq N_{H,z}/U_X n c$ s. Thus substituting our best-fitting values to the 1996 observations ($\langle N_{H,z} \rangle_{96}$ and $\langle U_X \rangle_{96}$), $t_{var} > t_{ion}$ if $n \gtrsim 3 \times 10^{12} t_{var}^{-1} \text{ cm}^{-3}$. The recombination timescale for a given ionic species is given by $t_{rec} = 1/\alpha_r(T)n$, where $\alpha_r(T)$ is the recombination coefficient for gas at an equilibrium temperature T . Assuming $\alpha_r(T)$ from Verner & Ferland (1996), for a given value of T , $t_{rec}(\text{OVIII})$ is a factor ~ 2 smaller than $t_{rec}(\text{OVII})$, and hence we require $n \gtrsim 3 \times 10^8 T^{0.5} t_{var}^{-1} \text{ cm}^{-3}$. Thus, for $t_{var} = 5 \times 10^4$ s (the approximate timescale in which factor ~ 2 changes in flux are observed, Fig. 1) and $T \sim 10^5$ K, we require $n \gtrsim 10^8 \text{ cm}^{-3}$ for equilibrium, consistent with the density assumed in our ION models. Using eqn.1, the derived value of $\langle L_{0.1-10} \rangle_{96}$ and $\langle U_X \rangle_{96}$, such densities require $r \lesssim 20$ light-days.

Our ION models also assume that the ionized material has no significant internal turbulence in excess of that predicted by the local sound speed. If such turbulence is in fact present, then features due to resonance-scattering may become visible in the spectrum. With such a scenario in mind we have also considered other parameterizations of the 1 keV deficit in the 1993 datasets. From Table 4 it can be seen that both 'notch' and gaussian models have energies in the range 0.9–1.1 keV. There are a number of resonance transitions in this band, the strongest of which are due to NeIX–X and FeXIX–XXI assuming cosmic abundances. It is possible that the 1 keV deficit is due to resonance-scattering by one or more of these species in a turbulent region (velocities $\gtrsim 0.02c$). However there are a large number of other resonance transitions throughout the 0.6–1.5 keV band. For the implied level of ionization, strong features would also be expected elsewhere (especially in the 0.6–0.9 keV band due to OVII–VIII). Given the resolution of *ASCA*, certain juxtapositions of such features can mimic a series of bound-free edges. Unfortunately it is not possible to determine what fraction of the opacity (if any) is due to resonance-scattering using the the current data.

Thus non-equilibrium and/or turbulent effects cannot be excluded, but we suggest they are unlikely to be solely responsible for the observed deficit.

4.3.4. *Is the emission from the gas important ?*

The ionized material responsible for the absorption features will also give rise to emission features due to bound–bound and recombination transitions. In addition, electrons in the gas will scatter the continuum. Hence if the material subtends a significant solid angle (Ω) as seen from the central source, such components may be visible in the observed spectrum. For the values of $N_{H,z}$ and U_X implied in the case of NGC 3783, the most prominent of these features within the *ASCA* bandpass are the OVII(568–574 eV) and OVIII(654 eV) emission lines (e.g. Netzer 1996). We have repeated the spectral analysis assuming an ionized absorber and the spectrum expected from the corresponding ‘photoionized-emitter’. The values of $N_{H,z}$ and U_X of the emitting gas were fixed to be the same as for the absorbing material (hence giving only one additional parameter, Ω , compared to the model used for Table 3).

In the case of the 1996 datasets, we find a negligible improvement in the quality of the fit compared to the model without the ionized–emitter ($\Delta\chi^2 \lesssim 2$ in all cases). At 90% confidence (for 1 interesting parameter) we find $\Omega/4\pi \leq 0.48$. Significant improvements in the quality of the fits are obtained by including the ionized–emitter in the 1993 datasets (at > 99% confidence using the *F*-test in the case of Obs.a). We find the allowed range in $\Omega/4\pi$ to be 0.6–1.0 and 0.3–0.8 (at 68% confidence for 4 interesting parameters) for Obs.a and b (respectively). However, in the case of Obs.a, the best-fitting model introduces positive residuals in the data/model ratio in the 0.5–1 keV band, not previously present. Thus we cannot explain the 1 keV deficit without introducing other deviations between model and data. Thus we do not consider this a satisfactory explanation of the discrepancies between the data and models.

4.3.5. *Is the absorber patchy ?*

If the screen of ionized material is patchy, then the observer may have lines-of-sight to the nucleus which undergo different degrees of attenuation. We tested such an hypothesis by first allowing a fraction of the nuclear emission to be observed without any attenuation (besides $N_{H,0}^{gal}$ due to our galaxy). If more than a few percent of the nuclear emission escapes absorption, then this effect might be detectable in the *ASCA* data. However, this extra degree of freedom produced no improvement to the fits. We also tested a model in which a fraction of the continuum is attenuated by ionized gas with U_x and $N_{H,z}$ whilst the remainder is attenuated by material with a different U_x and/or $N_{H,z}$. However even this more complex model produced no significant improvement to the fits. Thus we conclude that the 1 keV deficit is not the artifact of a patchy absorber.

4.3.6. Are there two (or more) zones of ionized gas ?

Another possibility is that there are two (or more) zones of ionized material surrounding the nucleus, and that the transmission of radiation through one zone and then the next, yields a different spectral shape to transmission through a single-zone of gas. In this case, the simplest picture is that one of the zones is responsible for the bulk of the opacity during the 1996 observations and is also present during the 1993 observations. Thus this zone, with a column density $\langle N_{H,z} \rangle_{96}$, can be considered the 'ambient' gas. During the 1996 observations, an additional zone (cloud) is responsible only for the small 1 keV deficit evident in Fig. 3. However during the 1993 observations, the additional zone contributes significant opacity as demonstrated in Fig. 4. Thus both zones are required for both epochs, but a significant change is only required in one of the zones, to explain the observed variations in opacity.

It is difficult to constrain any two-zone, ionized-absorber using these *ASCA* data, and additional complexity arises since one must consider the relative covering fractions, cloud sizes, radii and densities of the two zones. As a full treatment of the two-zone case is beyond the scope of this paper, we make a simple parameterization of the attenuation in excess of the 'ambient layer', by adding the expected absorption edges to the model for the 1993 data. We assume the ambient absorber dominates the 1996 absorption, and fix its column density at $\langle N_{H,z} \rangle_{96} = 1.33 \times 10^{22} \text{ cm}^{-2}$. We assume this zone of gas responds simply to changes in the source flux, and thus we have calculated and fixed the ionization parameter of the ambient absorber for each 1993 dataset assuming $U_X = \langle U_X \rangle_{96} \times (L_{0.5-2} / \langle L_{0.5-2} \rangle_{96})$ where $\langle U_X \rangle_{96}$ and $\langle L_{0.5-2} \rangle_{96}$ are from our analysis above. The threshold energies of the absorption edges were fixed at the appropriate values, and those with some evidence for non-negligible values of τ are listed in Table 5. It can be seen that as expected OVIII is the dominant feature in the second absorber. The depth of this extra edge, $\tau(\text{OVIII}) \simeq 0.6_{-0.2}^{+0.2}$, implies a column density in OVIII $\simeq 6_{-2}^{+2} \times 10^{18} \text{ cm}^{-2}$. For cosmic abundances, and allowing for the unknown fraction of fully-stripped O, this implies an effective hydrogen column density in this second zone $\gtrsim 10^{23} \text{ cm}^{-2}$. Excess OVIII can also explain the smaller 1 keV deficit in the 1996 data, in this case $\tau(\text{OVIII}) \simeq 0.15$ (Table 4). Thus, in the context of the two zone model, the column in the second zone dropped by a factor of ~ 4 between the 1993 and 1996 epochs.

5. SPECTRAL ANALYSIS OF THE IRON *K*-SHELL EMISSION

It is clear from the data/model residuals shown in Figs. 3, 4 and 5 that the spectrum of NGC 3783 contains a strong emission component in the 5–7 keV band at both epochs. Such

a feature is very common in Seyfert galaxies and interpreted in terms of a $K\alpha$ fluorescence line from Fe (e.g. Nandra & Pounds 1994). Furthermore, it can be seen that there is some indication that the line is asymmetric, skewed to lower energies in at least some of the datasets. Recent *ASCA* observations have shown such asymmetries are common in Seyfert galaxies (e.g. Nandra et al 1997b; Turner et al 1998, and references therein), and have been interpreted to arise as the result of the extreme Doppler and gravitational effects suffered by line photons emitted close to the putative black hole (Mushotzky et al 1995; Tanaka et al 1995).

As noted above, the best-fitting parameters of the emission line are dependent upon the form of the underlying continuum. Since the best-fitting continuum is correlated with the absorption present in the soft X-ray band, we have repeated the spectral analysis, but now also including the data within the 5–7 keV band. Thus we have taken a model consisting of an underlying powerlaw, an ionized-absorber, and have added spectral components to model the Fe emission. For simplicity we have used the single-zone model for the ionized absorber. This leads to the re-introduction of the 1 keV deficit, but we believe such an approach provides a good estimation of the opacity, and hence slope of the continuum in the 5–7 keV band.

In order to keep our analysis as unbiased as possible, we chose to parameterize the Fe $K\alpha$ emission as a combination of the emission expected from the innermost regions of the putative accretion flow and a narrow (< 10 eV) component appropriate for near-neutral Fe. We also include the Fe $K\beta$ emission assuming an intensity 10% of that of the corresponding $K\alpha$ component. The Fe emission from the innermost regions of the accretion flow was parameterized following Fabian et al. (1989). Namely we calculate the profile for a line of rest-frame energy E_z assuming a planar geometry where the inclination of our line-of-sight with respect to the normal to the plane is given by i , and in which the line emissivity as a function of radius (r) from a Schwarzschild black hole is proportional to r^{-q} over the range $R_i < r < R_o$, and zero elsewhere. Below we refer to this component as the ‘diskline’ emission. The narrow component was included with rest-energies of 6.4 keV and 7.06 keV for Fe $K\alpha$ and $K\beta$ (respectively) to allow for the possibility of other structures in the circumnuclear environment of the AGN. Such structures (for example the outer regions of the accretion flow, the putative molecular torus, etc) could be sufficiently distant that relativistic effects are unimportant and Fe is in a near-neutral state ($< \text{FeXIII}$), yet still subtend a sufficient solid angle at the central source to contribute to the Fe emission observed.

As in §4.2, we first discuss our results from the 1996 observations, and then compare these to the 1993 observations.

5.1. The 1996 observations

Unfortunately we are unable to constrain all the parameters associated with the diskline component using the individual datasets. Thus, as above we have chosen to analyse all the datasets obtained during 1996 simultaneously. Fixing R_i at $6r_g$ (where $r_g = GM/c^2$ is the gravitational radius of the black hole of mass M), appropriate for the innermost stable orbit within the Schwarzschild metric, we find best-fitting inclination $i = 26_{-12}^{+12}$ degrees (at 68% confidence for 9 interesting parameters). The best-fitting value of q pegged at the largest value ($q = 3$), although values over the entire range allowed $0 \leq q \leq 3$ are acceptable at 90% confidence. The equivalent widths of the $K\alpha$ lines are $EW_{dl} = 230 \pm 60$ eV and $EW_{nl} = 60 \pm 20$ eV (at 68% confidence for 2 interesting parameters). Fig.6 shows the data/model ratio in the iron K regime, illustrating the implied line profile, compared to the model described above. Given the steepness of the implied emissivity, R_o could not be constrained and we therefore consider it uninteresting.

From Fig.6 it can be seen that there is significant Fe $K\alpha$ emission bluewards of 6.4 keV. Indeed the best-fitting value of diskline energy is $E_z = 6.962$ keV for the $K\alpha$ component, indicative of FeXXVI. However the 90% confidence range for 9 interesting parameters extends down to 6.4 keV. In any case, the narrow component of the line could be from highly ionized iron, while the diskline is from neutral material. As the narrow component is too strong to arise from the warm absorber, the former suggestion seems the most compelling. We find the inclusion of the narrow line component provides a significant improvement to the fit ($\Delta\chi^2 = 19$). Excluding this component could lead us to the wrong conclusion as to the detailed shape of the diskline, thus it is also included below when fitting the 1993 data. Consideration of the Compton-reflection component, with an inclination equal to that of the diskline, yields a constraint $\Omega_R/2\pi < 1.5$ on the solid angle subtended to the continuum source.

The spectral fits which included this consideration of the Fe K -shell regime found best-fitting values of $N_{H,z}$, U_X and Γ gas as found in §4.2.

5.2. The 1993 observations

In the lower two panels of Fig.6 we compare the 1993 data with the composite line profile obtained from fitting the 1996 data. This shows that both the shape and equivalent width of the iron line are consistent with the 1996 data. This was confirmed by fits to the 1993 data. Again, the parameters associated with the ionized absorber ($N_{H,z}$ and U_X) were consistent with those found in §4.2.

6. SUMMARY & CONCLUSIONS

6.1. The ionized-absorber

Our observations confirm the presence of substantial opacity due to ionized material within the column-of-sight to the X-ray emitting region in NGC 3783. Furthermore we have found this opacity in the $\sim 0.7\text{--}1.0$ keV band to decrease by a factor ~ 2 in the 18 months between the observations carried out in 1993 and 1996. This large change in opacity is inconsistent with that expected if the ionized material is simply responding to changes in the illuminating continuum. Such behaviour has been seen in at least two other objects (MCG-6-30-15, Fabian et al 1994; NGC 3227, Ptak et al 1994, George et al 1998b).

During both epochs we find the bulk of the opacity to be reasonably well modelled by a screen of ionized material. However, in all cases, we find a deficit is present in the data/model residuals. In §4.3 we briefly explored a number of possible explanations for such a deficit. We suggest that the most attractive explanation is in terms of there being two or more zones of photoionized material (§4.3.6). In this case the column variability can be attributed to a change in column of just one of the zones, which might then be inferred to exist as clouds moving into and out of the column-of-sight. Such an hypothesis has been suggested in other objects based on the differential variability in the depth of the OVII and OVIII edges (e.g. NGC 3227, Ptak et al 1994; MCG-6-30-15, Otani et al 1996; NGC 4051, Guainazzi et al 1996), and/or, as here, spectroscopically based on detailed photoionization calculations (e.g. NGC 3516, Kriss et al 1996). Of course future observations will reveal whether the zone referred to as the 'ambient gas' in §4.3.6 truly always lies within the column-of-sight. A viable alternative is that this zone is in fact simply a slower moving (or larger) structure traversing the the column-of-sight.

Absorption features due to CIV, NV and possibly HI have been observed in the ultraviolet (UV) spectrum of NGC 3783 (e.g. Shields & Hamann 1997, and references therein). Furthermore there is good evidence that the implied column density in these ions is variable (e.g. Maran et al 1996). Based on the column densities implied by the 1993 *ASCA* observations of the OVII and OVIII edges as given in G95, Shields & Hamann demonstrated that the predicted column densities in the UV absorption lines to be in moderately good agreement with the observed range. Hence it was suggested that there might be a single zone of ionized material responsible for the absorption features in both the X-ray and UV regimes. Since the UV absorption due to CIV is seen imprinted on the corresponding broad emission line, this would clearly place the location of the ionized material at a radius larger than the region emitting the bulk of the broad CIV emission (\gtrsim several light-days). This is in agreement with our estimate in §4.3.3 that the material

had to be at a radius $\lesssim 20$ light-days in order to be in ionization equilibrium. In Table 6 we list the column densities of the abundant Li-like ions predicted from our single-zone model of the ambient gas implied by the *ASCA* observations in 1996. We find column densities in the strong UV absorption lines within an order of magnitude of those observed, confirming the basic conclusion of Shields & Hamann. However, as acknowledged by Shields & Hamann and several other workers (e.g. Mathur 1997 and references therein), such comparisons are extremely sensitive to the form of the photoionizing continuum in the unobserved 13.6–300 eV band, and the assumed elemental abundances. Given these facts, and the observed variability, more detailed comparisons require simultaneous X-ray and UV observations of a wider species of ions such as may be possible with the launch of *AXAF*, *XMM* and *FUSE*.

Unfortunately, due to the uncertainties in the calibration of the XRT/SIS instrument below 0.6 keV (and hence our exclusion of these data from our detailed spectral analysis) our data are unable to provide stringent constraints on the intensity of the emission features predicted to arise within the ionized material. However, as noted in §4.3.4, the limits provided by the current data are consistent with the material subtending a solid angle $\lesssim 2\pi$ at the central source.

6.2. The Fe emission line

Our data confirm the presence of intense Fe *K*-shell emission within NGC 3783, with a total equivalent width (~ 300 eV) and broad, asymmetric profile fairly typical of other Seyfert 1 galaxies (e.g. Nandra et al 1997b, and references within). In §5 we suggest the line can be deconvolved into two components. The first is a narrow component with a rest-frame energy of 6.4 keV (corresponding to an ionization state $\lesssim \text{FeXII}$) with an equivalent width (~ 60 eV) consistent with production within the distant structures within the circumnuclear environment of the central source (Ghisellini, Haadt, Matt 1994). The second component, referred to as the diskline component in §5, is that arising close to 6 gravitational radii of a putative supermassive black hole. The extreme gravitational effects suffered by the emission line photons at such radii give rise to an asymmetric profile. We find no compelling evidence that the Fe emission varied in either shape or equivalent width between the 1993 and 1996, indicating no significant changes in the distribution of Fe emissivity.

We thank Tahir Yaqoob, Fred Hamann and Joe Shields for useful discussions. We acknowledge the financial support of the Universities Space Research Association (IMG, TJT), National Research Council (KN), and the US-Israel Binational Science Foundation

and NASA (NH). This research has made use of the Simbad database, operated at CDS, Strasbourg, France; and of data obtained through the HEASARC on-line service, provided by NASA/GSFC.

REFERENCES

- Alloin, D., et al. 1995, A&A, 293, 293
- Burke, B.E., Mountain, R.W., Daniels, P.J., Dolat, V.S., 1994, IEEE Trans. Nuc. SCI., 41, 375
- Fabian, A.C., Rees, M.J., Stella, L., White, N.E., 1989, MNRAS, 238, 729
- Fabian, A.C., et al, 1994, PASJ, 46, L59
- George, I.M., Turner, T.J., Netzer, H., 1995, ApJ, 438, L67 (G95)
- George, I.M., Netzer, H., Turner, T.J., Nandra, K., Mushotzky, R.F., Yaqoob, T., 1998a, ApJS 114, 73 (G98)
- George, I.M., Turner, T.J., Nandra, K., Mushotzky, R.F., Yaqoob, T., Ptak, A., Netzer, H., 1998b, in preparation
- Ghisellini, G., Haardt, F., Matt, G., 1994, MNRAS, 267, 743
- Gotthelf, E.V., Ishibashi, K., 1997, in *X-ray Imaging and Spectroscopy of Cosmic Hot Plasmas* (Tokyo: Universal Academy Press) eds. Makino, F., Mitsuda, K., p631
- Guainazzi, M., Mihara, T., Otani, C., Matsuoka, M., 1996, PASJ, 48, 781
- Kriss, G.A., et al., 1996, ApJ, 467, 629
- Makishima, et al 1996, PASJ, 48, 171
- Mathur, S., 1997, in *Mass Ejection from AGNs*, eds Arav, N., Shlosman, I., Weymann, R.J., (San Francisco: Astronomical Society of the Pacific), p161
- Malizia, A., Bassani, L., Stephen, J.B., Malaguti, G., Palumbo, G.G.C., 1997, ApJS, 113, 311
- Maran, S.P., Crenshaw, D.M., Mushotzky, R.F., Reichert, G.A., Carpenter, K.G., Smith, A.M., Hutchings, J.B., Weymann, R., 1996, ApJ, 465, 733
- Mushotzky, R.F., Fabian, A.C., Iwasawa, K., Kunieda, H., Matsuoka, M., Nandra, K., Tanaka, Y., 1995, MNRAS, 272, L9
- Nandra, K., Pounds, K.A., 1994, MNRAS, 268, 405
- Nandra, K., George, I.M., Mushotzky, R.F., Turner, T.J., Yaqoob, T., 1997a, ApJ, 476, 70
- Nandra, K., George, I.M., Mushotzky, R.F., Turner, T.J., Yaqoob, T., 1997b, ApJ, 477, 602
- Netzer, H., 1993, ApJ, 411, 594
- Netzer, H., 1996, ApJ, 473, 781
- Ohashi, T., et al, 1996, PASJ, 48, 157

- Otani, C., et al., 1996, PASJ, 48, 211
- Ptak, A., Yaqoob, T., Serlemitsos, P.J., Mushotzky, R.F., Otani, C., 1994, ApJ, 436, L31
- Reynolds, C.S., 1997, MNRAS, 286, 513
- Serlemitsos, P.J., et al, 1995, PASJ, 47, 105
- Stark, A.A., Gammie, C.F., Wilson, R.W., Bally, J., Linke, R.A., Heiles, C., Hursitz, M., 1992, ApJS, 79, 77
- Shields, J.C., Hamann, F., 1997, ApJ, 481, 752
- Tanaka, Y., et al., 1995, Nature, 375, 659
- Turner, T.J., Nandra, K., George, I.M., Fabian, A.C, Pounds, K.A., 1993, ApJ, 423, 621
- Turner, T.J., George, I.M., Nandra, K., Mushotzky, R.F., 1998, ApJ, 493, 91
- Verner, D.A., Yakovlev, D.G., 1995, A&ASuppl, 109, 125
- Verner, D.A., Ferland, G.J., 1996, ApJS, 103, 467

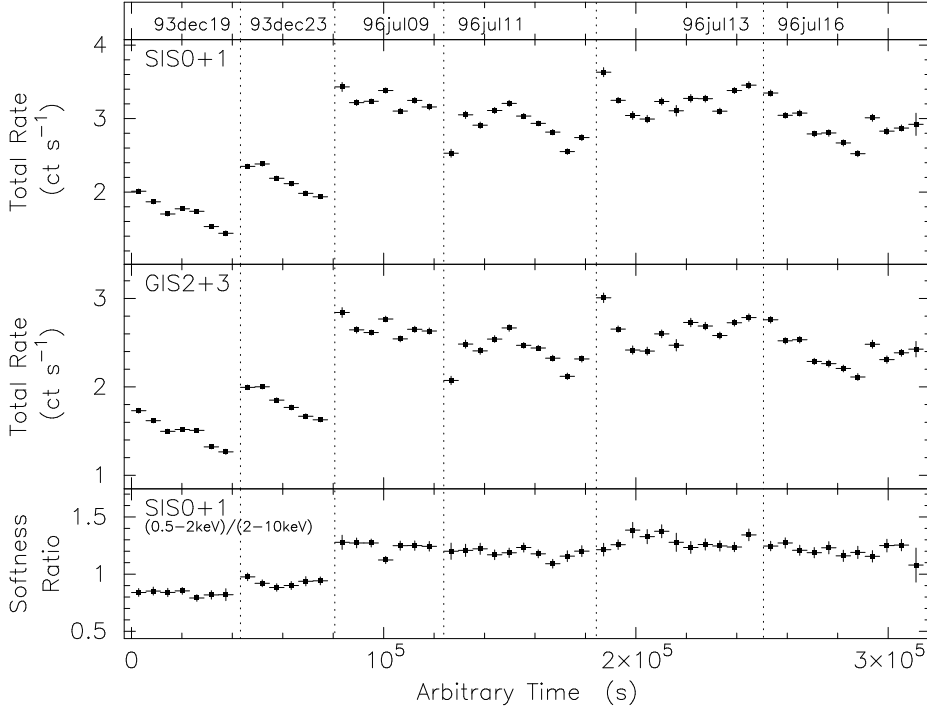


Fig. 1.— Light curves for the six *ASCA* observations of NGC 3783 reported here, employing a bin size of 5760 s. The upper two panels show the summed light curves obtained for SIS and GIS detectors, whilst the lower panel shows the softness ratio (the ratio of the summed count rates observed in the 0.5–2 keV and 2–10 keV bands) for the SIS detectors. In all cases, the y-axis is scaled to cover a factor of 0.4 to 1.6 of the mean. Significant variability is clearly apparent in the observed count rates both within the individual observations, and between the 1993 and 1996 epochs. However, whilst there is a clear change in the softness ratio between the 1993 and 1996 observations, there is no evidence for significant variability in this quantity within individual observations.

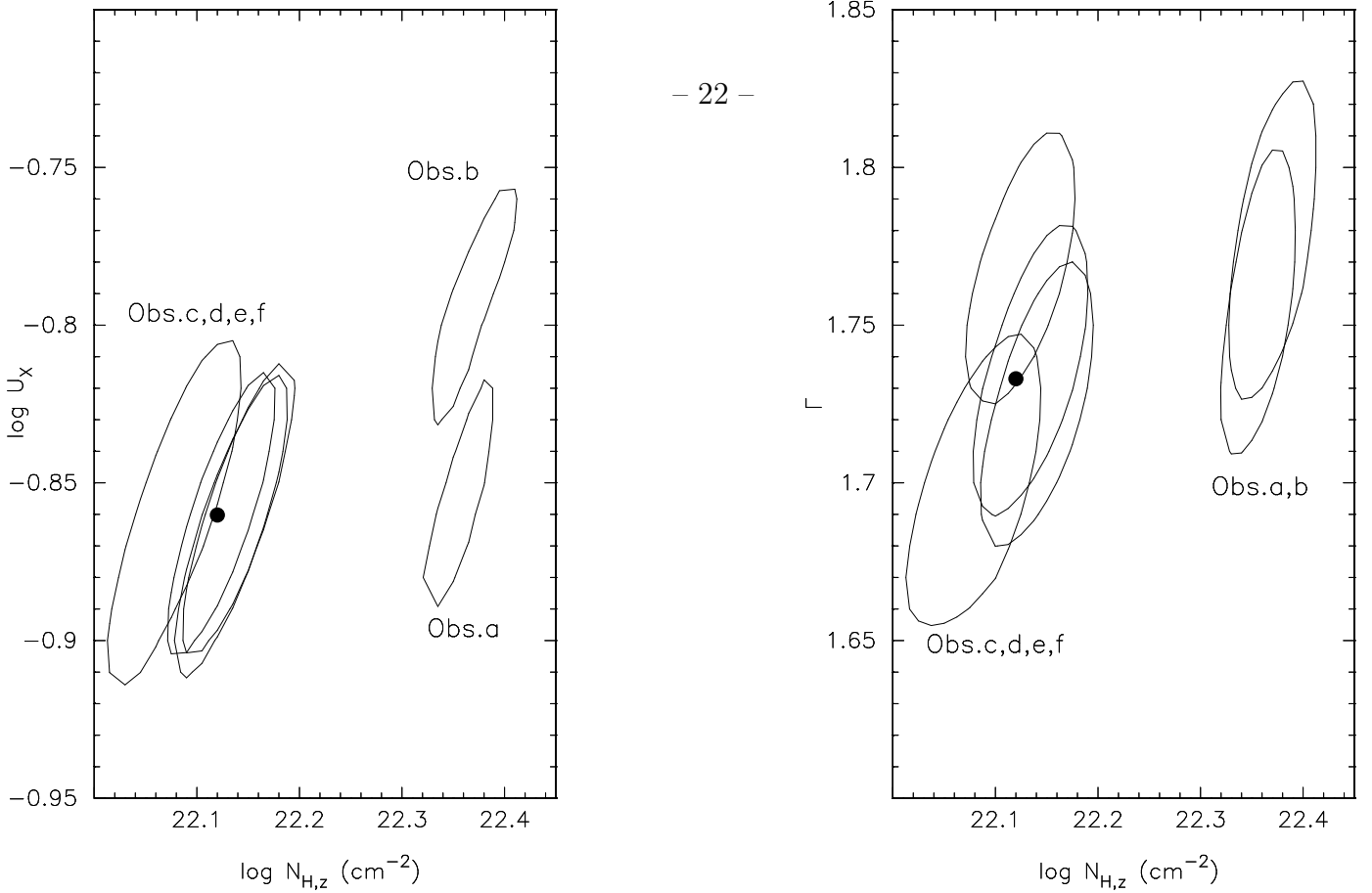
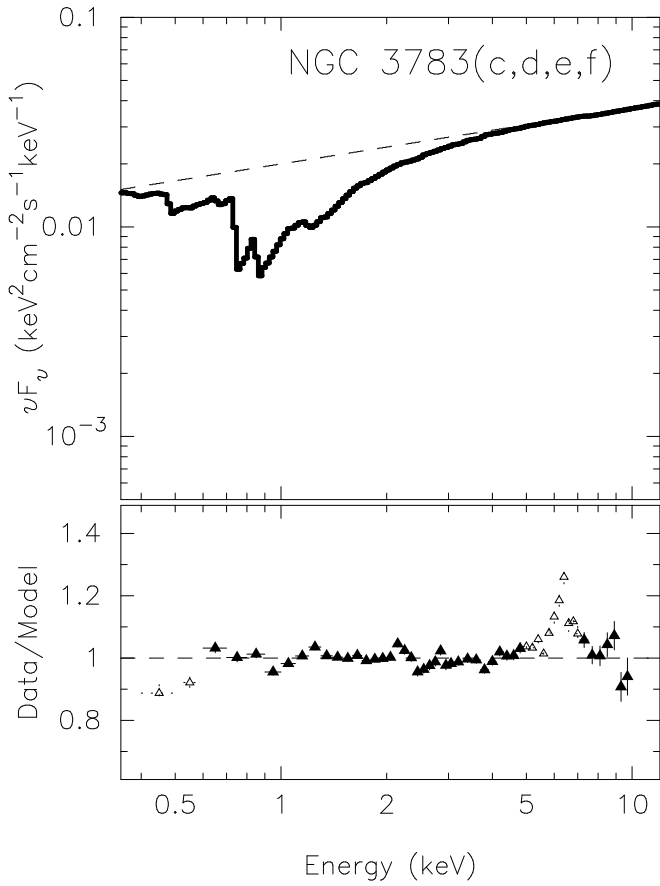


Fig. 2.— Contours showing the 90% confidence regions (for 3 interesting parameters) in the $N_{H,z}$ - U_X and $N_{H,z}$ - Γ planes for each of the observations of NGC 3783 assuming a model consisting of an underlying powerlaw continuum, a single-zone ionized absorber and with $N_{H,0} = N_{H,0}^{gal}$. As also apparent from Table 3, all four datasets obtained in 1996 (Obs.c – f) are consistent with mean values of $\langle N_{H,z} \rangle_{96} = 1.32 \times 10^{22} \text{ cm}^{-2}$, $\langle U_X \rangle_{96} = 0.138$, and $\langle \Gamma \rangle_{96} = 1.73$ (denoted by the filled circle). A larger opacity is evident in the two datasets obtained in 1994 (Obs.a & b), although it should be noted that the assumed model does not provide a satisfactory description in these cases (see §4.2.2).



– 23 –

Fig. 3.— The upper panel shows (in bold) the best-fitting, single-zone photoionization model obtained from simultaneous spectral analysis of the *ASCA* observations obtained during 1996 (see §4.2.1), along with (dashed) the implied underlying continuum. Both curves have been corrected for Galactic absorption ($N_{HI}^{Gal} = 8.7 \times 10^{20} \text{ cm}^{-2}$). The model represents a powerlaw continuum of photon index $\langle \Gamma \rangle_{96} = 1.73$ absorbed by a screen of ionized material within the column-of-sight of column density $\langle N_{H,z} \rangle_{96} = 1.32 \times 10^{22} \text{ cm}^{-2}$ and ionization parameter $\langle U_X \rangle_{96} = 0.138$. The lower panel shows the mean data/model ratios. The filled triangles show the (error-weighted) means of the ratios from the individual detectors for the energy-bands used in the spectral analysis, rebinned in energy-space for clarity. The open triangles show the corresponding rebinned, mean ratios when the best-fitting model is extrapolated $< 0.6 \text{ keV}$ and into the 5–7 keV band. As noted in §4.2.1, there are four major discrepancies between the data and model: the Fe *K*-shell emission (discussed in §5), the instrument features $< 0.6 \text{ keV}$ and in the 2–3 keV band, and the ‘1 keV deficit’ (discussed in §4.3).

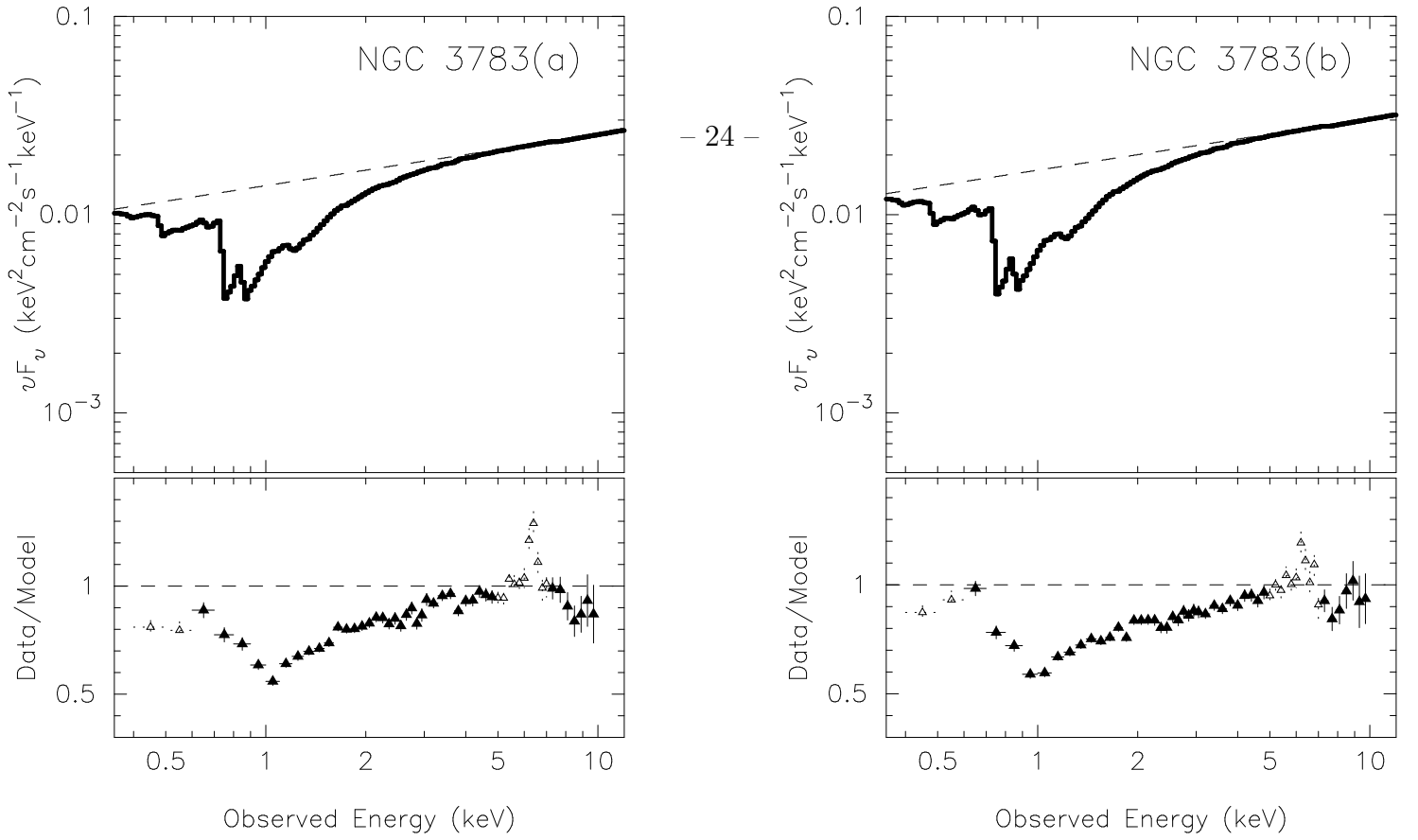


Fig. 4.— The mean data/model ratios residuals for the 1993 observations of NGC 3783 (with symbols as for Fig. 3) assuming an underlying photon index $\langle \Gamma \rangle_{96} = 1.73$, a screen of ionized material within the column-of-sight of column density $\langle N_{H,z} \rangle_{96} = 1.32 \times 10^{22} \text{ cm}^{-2}$ and where the ionization parameter during each observation is given by (see §4.2.2) $U_X = 0.138(L_{0.5-2}/2.07 \times 10^{43} \text{ erg s}^{-1})$. Excess opacity is clearly evident indicating different gas is contributing to the the 1993 observations compared to the 1996 observations.

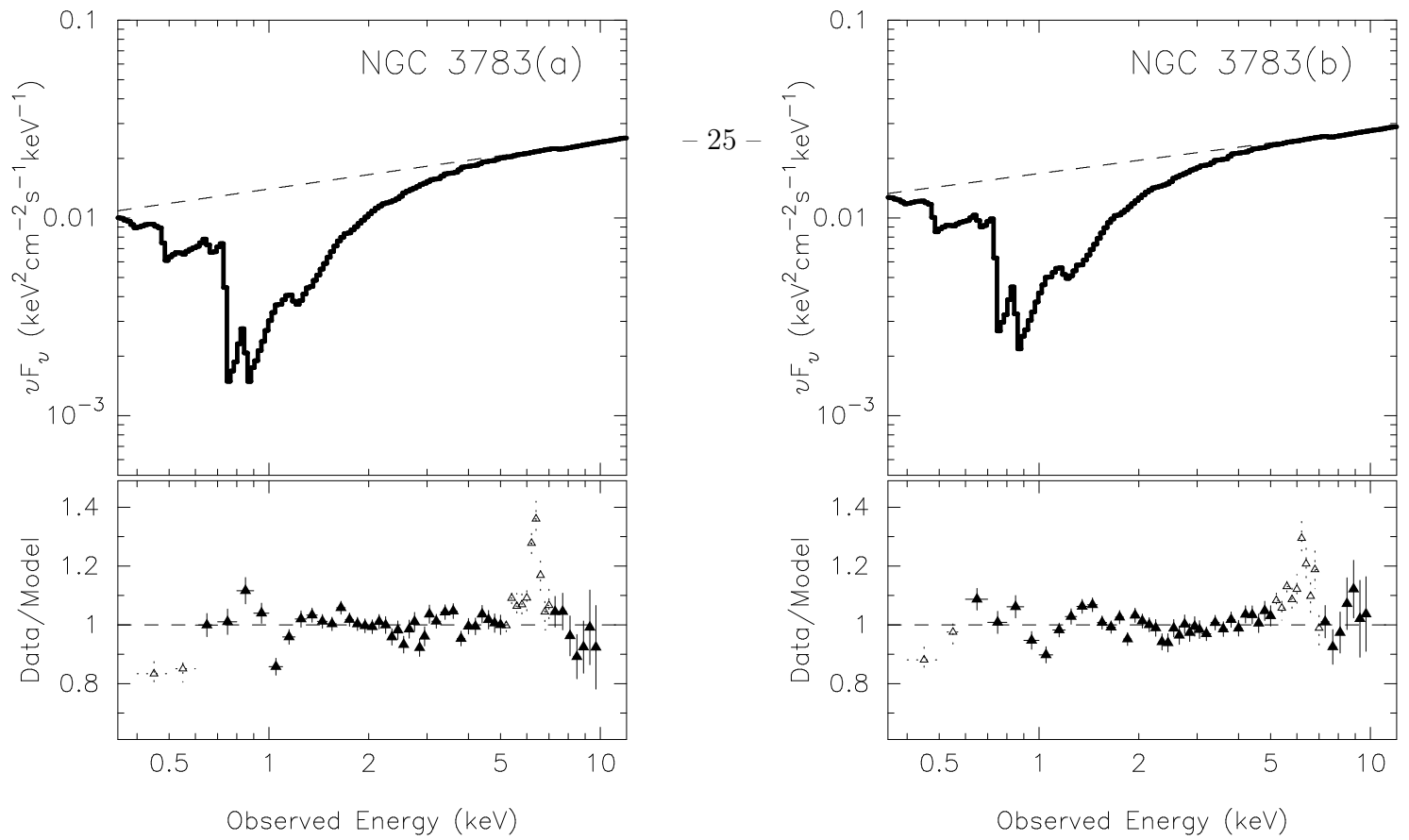


Fig. 5.— As for Fig. 3, showing the best-fitting, single-zone photoionization model obtained from the spectral analysis of the individual *ASCA* observations obtained during 1993 (see §4.2.2). It should be noted that despite explaining the bulk of the opacity, a '1 keV deficit' is clearly present, and is deeper than that present in the fits to the 1996 data (Fig. 3).

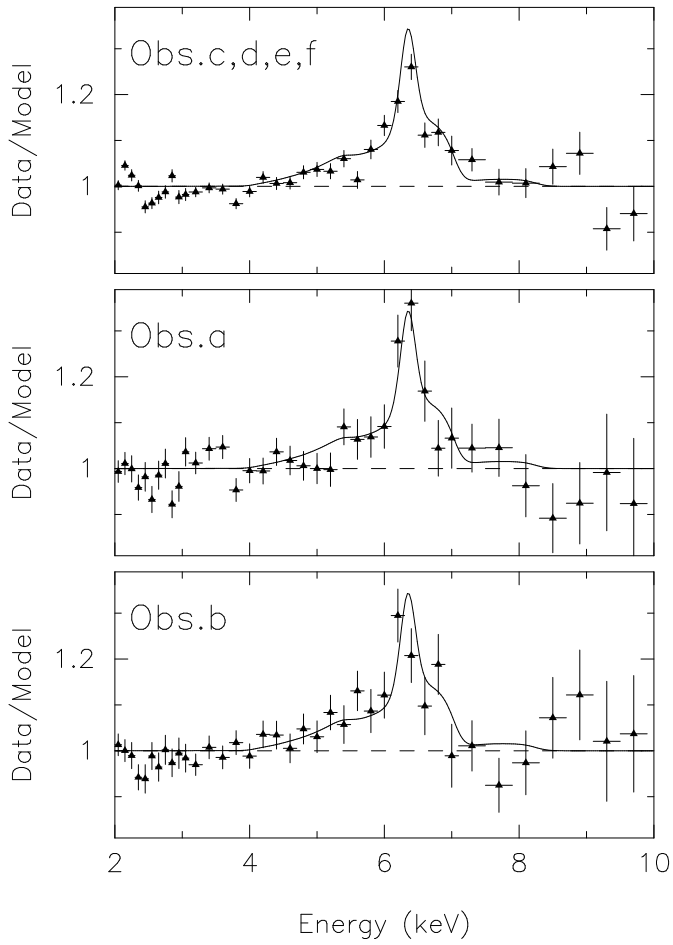


Fig. 6.— The filled points show the mean data/model ratios in the Fe K -shell regime assuming the best-fitting models described in §4.2. In all three panels the solid line shows the best-fitting parameterization of the Fe emission to the 1996 data (as discussed in §5) convolved with the spectral response of the SIS detectors. It is clear that there is no significant evidence for a change in either shape or equivalent width of the Fe emission.

TABLE 1
OBSERVATION LOG OF THE *ASCA* OBSERVATIONS OF NGC 3783

Obs.	Seq. No.	Date	CCD mode	$t_{exp}(\text{SIS0})$ (10^3 s)	$Rate(\text{SIS0})$ (count s^{-1})	N_{pts} (excl 5–7 keV)	F_{2-10} (10^{-12} erg cm^{-2} s^{-1})
(1)	(2)	(3)	(4)	(5)	(6)	(7)	(8)
a	71041000	1993 Dec 19	2	17.3	0.940 ± 0.008	1038	57.7 ± 2.9
b	71041010	1993 Dec 23	2	15.0	1.117 ± 0.009	1017	67.1 ± 3.4
c	74054000	1996 Jul 09	1	14.9	1.677 ± 0.011	1091	88.3 ± 4.4
d	74054010	1996 Jul 11	1	18.7	1.487 ± 0.009	1098	80.4 ± 4.0
e	74054020	1996 Jul 14	1	15.5	1.671 ± 0.011	1082	86.0 ± 4.3
f	74054030	1996 Jul 16	1	16.6	1.512 ± 0.010	1089	80.7 ± 4.0

NOTE.— Col.(1): The observation code used throughout this work. Col.(2): *ASCA* sequence number. Col.(3): Observation date (start of exposure). Col.(4): Clocking mode used for the SIS CCDs. Col.(5): Total exposure time of selected data (for SIS0). Col.(6): Mean SIS0 count rate in the 0.6–10.0 keV band. Col.(7): Number of spectral data points (summed over all four instruments) in the 0.6–5.0, 7.0–10.0 keV band used in the spectral analysis presented in §4. Col.(8): Observed flux in the 2–10 keV band assuming 5% errors.

TABLE 2
 VARIABILITY AMPLITUDE ($10^{-2}\sigma_{rms}^2$) FOR NGC 3783

Obs.	SIS Full (0.5–10 keV)	SIS Soft (0.5–2 keV)	SIS Hard (2–10 keV)	GIS Hard (2–10 keV)
(1)	(2)	(3)	(4)	(5)
a	0.97 ± 0.15	1.02 ± 0.24	0.94 ± 0.19	0.76 ± 0.15
b	0.62 ± 0.12	0.60 ± 0.19	0.45 ± 0.15	0.70 ± 0.13
c	0.07 ± 0.05	0.11 ± 0.08	0.15 ± 0.11	0.16 ± 0.07
d	0.64 ± 0.11	1.00 ± 0.21	0.29 ± 0.12	0.43 ± 0.12
e	0.18 ± 0.06	0.21 ± 0.10	0.28 ± 0.12	0.32 ± 0.09
f	0.65 ± 0.13	0.59 ± 0.13	0.78 ± 0.23	0.59 ± 0.11

NOTE.— Col.(1): The observation code. Cols.(2–5): Normalized excess variance, σ_{rms}^2 , and associated error calculated using the prescription of Nandra et al (1997a) from light curves with a binsize of 128 s.

TABLE 3
RESULTS FOR A SINGLE-ZONE IONIZED ABSORBER (SEE §4.2)

Obs	Γ	$N_{H,z}$ (10^{22} cm^{-2})	U_X	χ^2	P	$\frac{\Delta\chi_{0.6}^2}{\Delta N_{0.6}}$	$\overline{R_{0.6}}$	$L_{0.1-10}$ ($10^{43} \text{ erg s}^{-1}$)	$L_{0.5-2}$ ($10^{43} \text{ erg s}^{-1}$)	L_{2-10} ($10^{43} \text{ erg s}^{-1}$)
(1)	(2)	(3)	(4)	(5)	(6)	(7)	(8)	(9)	(10)	(11)
a	$1.76^{+0.04}_{-0.04}$	$2.29^{+0.14}_{-0.16}$	$0.139^{+0.011}_{-0.008}$	1134	0.99	2.6	0.84	5.25 ± 0.04	1.50 ± 0.01	2.53 ± 0.02
b	$1.78^{+0.04}_{-0.04}$	$2.34^{+0.20}_{-0.16}$	$0.167^{+0.006}_{-0.016}$	1113	0.99	1.8	0.93	6.15 ± 0.04	1.77 ± 0.01	2.94 ± 0.02
c	$1.70^{+0.04}_{-0.03}$	$1.23^{+0.12}_{-0.15}$	$0.140^{+0.012}_{-0.013}$	1111	0.72	2.1	0.99	7.26 ± 0.05	2.03 ± 0.01	3.70 ± 0.04
d	$1.73^{+0.03}_{-0.04}$	$1.38^{+0.14}_{-0.12}$	$0.139^{+0.011}_{-0.011}$	1113	0.68	5.3	0.82	6.84 ± 0.05	1.94 ± 0.02	3.40 ± 0.04
e	$1.77^{+0.03}_{-0.04}$	$1.35^{+0.12}_{-0.14}$	$0.138^{+0.012}_{-0.011}$	1153	0.95	2.9	0.92	7.66 ± 0.05	2.21 ± 0.01	3.64 ± 0.04
f	$1.74^{+0.03}_{-0.03}$	$1.38^{+0.12}_{-0.14}$	$0.137^{+0.012}_{-0.011}$	1127	0.83	2.6	0.93	6.95 ± 0.05	1.98 ± 0.01	3.42 ± 0.04
<i>weighted-mean values</i>										
a,b,c,d,e,f	1.75 ± 0.01	$1.55 \pm 0.05 \ddagger$	$0.151 \pm 0.004 \ddagger$	2.9	0.91	$6.49 \pm 0.01 \ddagger$	$1.90 \pm 0.01 \ddagger$	$3.12 \pm 0.01 \ddagger$
a,b	1.77 ± 0.03	2.31 ± 0.11	$0.161 \pm 0.005 \ddagger$	2.2	0.89	$5.70 \pm 0.02 \ddagger$	$1.64 \pm 0.01 \ddagger$	$2.74 \pm 0.01 \ddagger$
c,d,e,f	1.74 ± 0.02	1.33 ± 0.06	0.139 ± 0.006	3.2	0.92	$7.18 \pm 0.02 \ddagger$	$2.07 \pm 0.01 \ddagger$	$3.55 \pm 0.02 \ddagger$

NOTE.— Results from the fits undertaken in the 0.6–10.0 keV band (*excluding* the 5.0–7.0 keV band) assuming a powerlaw continuum absorbed by an ionized absorber at the redshift of the source, plus a neutral absorber with a column density fixed at the Galactic value ($N_{H,0}^{gal} = 8.7 \times 10^{20} \text{ cm}^{-2}$). The errors on the fit parameters are 68 per cent confidence limits for three interesting parameters. The mean values are calculated weighting the individual values using the reciprocal of the corresponding statistical error, with the variance on the mean calculated by the reciprocal of the sum of the weights. † best-fitting values inconsistent with a constant at >99% confidence. ‡ best-fitting values inconsistent with a constant at >95% confidence. Col.(1): The observation code(s). Col.(2): Photon index of the underlying continuum. Col.(3–4): Column density ($N_{H,z}$) and ionization parameter (U_X) of the ionized absorber. Col.(5): χ^2 -statistic for the fit for the N_{pts} data points given in Table 1. Col.(6): Probability that the χ^2 -statistic should be less than the observed value for the number of degrees of freedom, dof , given by $N_{pts} - 7$. Col.(7): Ratio of the increase in the χ^2 -statistic to the number of addition data points when the best-fitting model is extrapolated below 0.6 keV. Col.(8): Mean data/model ratio for data points below 0.6 keV. Cols.(9–11): Implied luminosity of the underlying continuum (excluding the Fe K-shell emission, and corrected for *all* absorption along the line-of-sight) over the 0.1–10, 0.5–2.0 and 2.0–10 keV energy ranges (respectively) assuming $H_0 = 50 \text{ km s}^{-1} \text{ Mpc}^{-1}$ and $q_0 = 0.5$.

TABLE 4
RESULTS FROM PARAMETERIZATIONS OF THE '1 KEV DEFICIT' (SEE §4.3)

Obs	Γ	$N_{H,z}$ (10^{22} cm $^{-2}$)	U_X	E_z	p1	p2	χ^2	P	$\frac{\Delta\chi^2_{0.6}}{\Delta N_{0.6}}$	$\overline{R_{0.6}}$
(1)	(2)	(3)	(4)	(5)	(6)	(7)	(8)	(9)	(10)	(11)
<i>edge model (p1=τ)</i>										
a	1.70 $^{+0.05}_{-0.05}$	1.66 $^{+0.30}_{-0.33}$	0.119 $^{+0.016}_{-0.018}$	0.871 (f)	0.51 $^{+0.23}_{-0.21}$...	1110	0.96	1.2	0.91
b	1.72 $^{+0.05}_{-0.06}$	1.66 $^{+0.37}_{-0.34}$	0.139 $^{+0.020}_{-0.018}$	0.871 (f)	0.47 $^{+0.21}_{-0.25}$...	1086	0.96	1.6	1.03
c,d,e,f	1.71 $^{+0.02}_{-0.02}$	1.10 $^{+0.15}_{-0.12}$	0.128 $^{+0.009}_{-0.009}$	0.871 (f)	0.15 $^{+0.07}_{-0.08}$...	4542	0.98	2.8	0.94
<i>notch model (p1=σ_n)</i>										
a	1.73 $^{+0.05}_{-0.05}$	2.19 $^{+0.21}_{-0.19}$	0.144 $^{+0.015}_{-0.012}$	1.06 $^{+0.02}_{-0.02}$	0.03 $^{+0.01}_{-0.01}$...	1091	0.92	2.2	0.86
b	1.76 $^{+0.05}_{-0.05}$	2.29 $^{+0.23}_{-0.25}$	0.164 $^{+0.014}_{-0.014}$	1.07 $^{+0.04}_{-0.05}$	0.02 $^{+0.01}_{-0.01}$...	1088	0.97	1.6	0.95
<i>gaussian model (p1=σ_g, p2=EW_g)</i>										
a	1.72 $^{+0.06}_{-0.06}$	2.19 $^{+0.21}_{-0.25}$	0.145 $^{+0.016}_{-0.013}$	1.07 $^{+0.03}_{-0.04}$	0.05 $^{+0.08}_{-0.05}$ (p)	40 $^{+2}_{-2}$	1090	0.91	2.0	0.86
b	1.73 $^{+0.06}_{-0.06}$	2.24 $^{+0.58}_{-0.26}$	0.174 $^{+0.050}_{-0.020}$	0.99 $^{+0.09}_{-0.14}$	0.12 $^{+0.10}_{-0.08}$	66 $^{+4}_{-9}$	1078	0.94	1.4	0.97

NOTE.— As for Table 3, but with the inclusion of an additional functional form to model the '1 keV deficit'. The first is an absorption edge, assuming a transmission of the form $\exp(-\tau(E/E_z)^{-2.67})$ for rest-frame energies $E \geq E_z$, and unity elsewhere (i.e. containing 2 additional parameters E_z and τ). The second is a 'notch', assuming zero transmission over an energy range $E_z - \sigma_n/2 \leq E \leq E_z + \sigma_n/2$ and unity elsewhere (i.e. 2 additional parameters). The third is a gaussian absorption feature, centered at an energy E_z , with a width σ_g , and equivalent width EW_g (i.e. 3 additional parameters). In all cases, E_z was constrained to lie within the range $0.6 \geq E_z \geq 1.362$ keV, corresponding to the lower cutoff energy in the datasets and the energy of the K -shell edge of Ne x (respectively). The allowed energies therefore cover the energies of bound-free K -shell transitions of N vii , O $v-viii$, and all species of Ne, along with a large number of bound-bound transitions in these species. Column headings as for Table 3, except cols.(5-7) which give the rest-frame energy (E_z) and additional parameters of the function modeling the 1 keV deficit.

TABLE 5
PARAMETERIZATION OF THE EXCESS OPACITY SEEN DURING 1993 (SEE §4.3.5)

Obs	Γ	$\tau(\text{OvIII})$	$\tau(\text{NeVIII})$	$\tau(\text{NeIX})$	$\tau(\text{Nex})$	$\tau(\text{Fe})$	χ^2	P	$\frac{\Delta\chi^2_{0.6}}{\Delta N_{0.6}}$	$\overline{R_{0.6}}$	$L_{0.1-10}$	$L_{0.5-2}$	L_{2-10}
(1)	(2)	(3)	(4)	(5)	(6)	(7)	(8)	(9)	(10)	(11)	(12)	(13)	(14)
a	$1.69^{+0.06}_{-0.05}$	$0.61^{+0.17}_{-0.19}$	$0.05^{+0.13}_{-0.05}$ (<i>p</i>)	$0.02^{+0.14}_{-0.02}$ (<i>p</i>)	$0.04^{+0.08}_{-0.04}$ (<i>p</i>)	$0.17^{+0.22}_{-0.17}$ (<i>p</i>)	1103	0.95	0.7	0.98	4.84 ± 0.03	1.36 ± 0.01	2.51 ± 0.02
b	$1.73^{+0.05}_{-0.04}$	$0.62^{+0.14}_{-0.14}$	$0.00^{+0.10}_{-0.00}$ (<i>p</i>)	$0.00^{+0.11}_{-0.00}$ (<i>p</i>)	$0.09^{+0.06}_{-0.07}$	$0.03^{+0.15}_{-0.03}$ (<i>p</i>)	1091	0.97	1.7	1.04	5.82 ± 0.03	1.65 ± 0.01	2.87 ± 0.02

NOTE.— Results from the model discussed in §4.3.5 in which a series of absorption edges are added to the opacity expected from the 1996 results. The ionization parameter was fixed at $U_X = 0.093$ & 0.112 for Obs.a & b respectively. In both cases $N_{H,z}$ is fixed at $1.32 \times 10^{22} \text{ cm}^{-2}$. Threshold energies of 0.871, 1.125, 1.125 & 1.362 keV were fixed for OvIII, NeVIII, NeIX & Nex respectively. The threshold energy for Fe were left free over the range 7.1–9.3 keV, and could not be constrained. The errors on the fit parameters are 68 per cent confidence limits for 7 interesting parameters. *p* indicates the parameter 'pegged' at the specified limit. Column headings as for Table 3, except cols.(3–7) which give the optical depth at the threshold energy of each edge.

TABLE 6
COLUMN DENSITIES OF INDIVIDUAL IONS FROM THE 1996 OBSERVATIONS

element	A/H (10^{-4})	$N_{ion} (\text{cm}^{-2})$		
(1)	(2)	Li-like (3)	He-like (4)	H-like (5)
C	3.63	2.0×10^{13}	8.1×10^{16}	1.3×10^{18}
N	1.12	4.0×10^{14}	1.3×10^{17}	6.8×10^{17}
O	8.51	5.9×10^{16}	3.0×10^{18}	5.3×10^{18}
Ne	1.23	1.4×10^{17}	8.6×10^{17}	3.8×10^{17}
Mg	0.38	1.5×10^{17}	2.5×10^{17}	3.9×10^{16}
Si	0.36	1.5×10^{17}	9.3×10^{16}	5.6×10^{15}
S	0.16	3.1×10^{16}	9.1×10^{15}	2.4×10^{14}
Ar	0.04	1.5×10^{15}	2.7×10^{14}	3.5×10^{12}

NOTE.— These predictions are for $U_X = 0.139$, $N_{H,z} = 1.32 \times 10^{22} \text{ cm}^{-2}$ and hence only for the 'ambient' material discussed in §4.3.5. It should be stressed that such values are very sensitive to the form assumed for the ionizing continuum in the XUV band (see text), and of course the elemental abundances. Col.(1): Atomic element. Col.(2): Assumed abundance relative to hydrogen. Cols.(3-5): Derived column density in the specified ion.